Near-Field Integrated Sensing and Communication for Multi-Target Indication

Hang Ruan [1], Homa Nikbakht [1,2], Ruizhi Zhang [1,3], Honglei Chen [4], Yonina C. Eldar [1]

[1]Weizmann Institute of Science, [2]Princeton University,
[3]University of Electronic Science and Technology of China, [4]MathWorks, Inc.
Emails: {hang.ruan, ruizhi.zhang, yonina.eldar}@weizmann.ac.il, homa@princeton.edu, h.chen@mathworks.com

***Abstract*—Integrated sensing and communication (ISAC) in the near-field regime offers the potential to jointly support high-rate downlink transmission and high-resolution multi-target detection by exploiting the spherical-wave nature of electromagnetic propagation. In this paper, we propose a unified beamforming framework for a multi-user multi-target near-field ISAC system. In this system, a multi-antenna base station simultaneously serves multiple single-antenna users and senses multiple point-targets without prior knowledge of their radar cross sections. By optimizing the transmit covariance matrix, our design maximizes the minimum weighted transmit beampattern gain across all targets to ensure accurate sensing while strictly limiting inter-target cross-correlations and guaranteeing per-user communication rate. We extend classical far-field beampattern and cross-correlation measures to the near-field by incorporating both angle and range dependencies, enabling discrimination of targets along the same direction but at different distances. The resulting non-convex program is efficiently relaxed to a semidefinite program via rank-one lifting. We then develop a closed-form reconstruction to recover optimal rank-one beamformers. Numerical simulations demonstrate that our near-field ISAC design can simultaneously resolve and serve users/targets along the same direction but at different distances, achieving significant gains over far-field and single-target benchmarks.**

I. Introduction

Integrated sensing and communication (ISAC) has emerged as a transformative paradigm that integrates communication and sensing functionalities into a single system, leveraging shared hardware and spectrum resources [1]. By enabling these dual functionalities, ISAC systems can enhance the efficiency of resource utilization, reduce hardware costs, and open new possibilities for applications such as autonomous vehicles, smart cities, and industrial automation [1].

In recent years, near-field communication and sensing have attracted growing interest, driven by the adoption of high-frequency systems and large-aperture multiple-input-multiple-output (MIMO) base station (BS) antennas [2]. In the near-field region, where the propagation distance is on the order of the Rayleigh distance, the spatial channels follow a spherical rather than planar wavefront. As a result, both communication and sensing channels depend on the users' or targets' angles and ranges [2], [3]. This range-dependent behavior enables the system to distinguish objects aligned in the same direction but at different distances, substantially improving spatial resolution for both functionalities [2], [3]. Such capabilities are essential for next-generation applications that demand high accuracy and spectral efficiency.

The design of multi-user, multi-target near-field ISAC systems, however, remains a significant challenge. Most existing studies on near-field ISAC beamforming focus on serving multiple communication users while sensing only a single target [2], [4]–[6], which severely limits performance in multi-target scenarios. To address this, recent works explore the multi-target problem. For instance, [3] considers multi-target sensing by treating echoes from other targets as interference and optimizes the signal-to-interference-plus-noise ratio (SINR) for each target. Separately, [7] formulate the beamforming design as a problem of minimizing the sum Cramér-Rao Bound (CRB) over all targets for localization, subject to communication quality-of-service constraints.

However, these existing multi-target approaches have two drawbacks. First, in MIMO sensing signal design, reducing cross-correlation among transmit waveforms is critical for accurate multi-target indication [8], [9] and for enabling adaptive MIMO radar techniques [10]. This requirement is not imposed in SINR-based method in [3], thereby deteriorating the capacity of multi-target indication. Second, both the SINR-based method in [3] and CRB-based method [7] assume prior knowledge of each target's radar cross-section (RCS) information to compute the respective performance metrics, yet RCS values are often unavailable in practical ISAC deployments. In contrast, evaluating sensing performance via beam-pattern gains and cross-correlation levels requires only known array steering functions and is entirely agnostic to RCS values [8]–[10].

Existing far-field MIMO beamforming designs treat each array's response as a function of direction only, using planar wavefront models with the steering vector varying solely with angle. As a result, classical ap-

proaches optimize both the transmit beampattern and the cross-correlation of waveforms over angular coordinates alone [8]–[10]. In the near-field, however, each antenna element sees a spherical wavefront whose strength and phase shift depend on both the distance to and the direction of each user or target. This means that two objects aligned along the same angle but at different ranges produce non-coherent channels. To exploit this, we generalize the traditional beampattern and cross-correlation criteria so that they account simultaneously for angle and range. Thus, our beamforming can not only form narrow beams in specific directions, but also focus or place nulls at particular distances, thereby enabling separation of users or targets that lie along the same direction but at different distances. This leads to greatly enhancement in both multi-user communications and multi-target sensing resolution in ISAC systems.

In this work, we propose a unified framework for joint transmit beamforming in near-field ISAC systems that simultaneously serves multiple downlink users and resolves multiple sensing targets without relying on prior RCS knowledge. By optimizing the transmitted signal covariance, our formulation maximizes the worst-case weighted beampattern gain across all targets while enforcing strict limits on mutual cross-correlation and guaranteeing per-user communication rate and total power constraints. Crucially, we extend classical far-field beampattern and cross-correlation metrics to depend on both angles and ranges, enabling the discrimination of objects at identical directions but different distances. To solve the resulting non-convex program, we recast it via semidefinite relaxation (SDR) into a convex form and derive a rank-one recovery procedure that yields optimal beamformers in closed form. Numerical results demonstrate that our method can simultaneously distinguish and serve users and sensing targets located in the same direction but at different distances.

Notations: Throughout the paper, $(\cdot)^T$, $(\cdot)^*$ and $(\cdot)^H$ denote transpose, conjugate and conjugate transpose, respectively; $\|\cdot\|$ is the Euclidean norm; $\mathrm{Tr}(\cdot)$ is the trace operator; $\mathbb{E}\{\cdot\}$ is statistical expectation; $\delta[\cdot]$ is the Kronecker delta function; and $\mathbf{I}_n$ is the $n \times n$ identity matrix. Scalars, vectors and matrices are denoted by italic, bold lowercase and bold uppercase letters.

II. System and Signal Model

A. System model

Fig. 1 illustrates the considered mmWave ISAC system. We assume a BS with a planar array of N_t antennas for transmission and another planar array of N_r antennas for sensing reception. The position of the n_t-th transmitting antenna element ($1 \le n_t \le N_t$) is denoted as $\boldsymbol{p}_t(n_t) \in \mathbb{R}^3$, with the array's radiation normal vector represented by $\boldsymbol{w}_t$, which defines the main direction of the array's radiation (i.e., its boresight). Analogously, the positions and radiation normal vector for the BS's receiving array are given by $\boldsymbol{p}_r(n_r)$ and $\boldsymbol{w}_r$, respectively.

The BS simultaneously serves downlink communication to K single-antenna users, indexed by the set $\mathcal{K}$, and senses L targets, indexed by the set $\mathcal{L}$. Each user/target $a \in \mathcal{K} \cup \mathcal{L}$ has a known position $\boldsymbol{p}_a$ within the near-field region of the BS, bounded by the Rayleigh distance $R_{\mathrm{RL}} = 2D^2/\lambda$ [2], where D is the antenna aperture, $\lambda = c/f_c$ is the wavelength, f_c is the carrier frequency, and c is the speed of light.

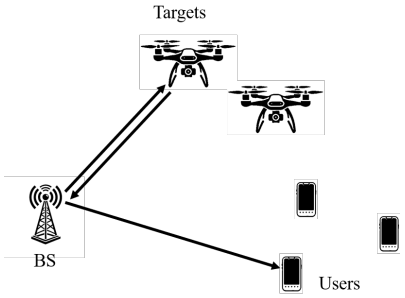

Fig. 1: Illustration of the near-field ISAC system with multiple communication users and multiple targets.

B. Transmitted ISAC signal

We consider a coherent block of length T. At time $t \in \{1, \ldots, T\}$, the transmitted signal of the BS is [11]

$$\boldsymbol{x}[t] = \sum\nolimits_{k\in\mathcal{K}} \boldsymbol{f}_k c_k[t] + \boldsymbol{s}[t], \tag{1}$$

where the n_t-th element of $\boldsymbol{x}[t] \in \mathbb{C}^{N_t}$ is the symbol transmitted by the n_t-th element ($1 \le n_t \le N_t$). The vector $\boldsymbol{f}_k \in \mathbb{C}^{N_t}$ is the fully digital beamformer for communicating the symbol $c_k[t]$ to the user k, and $\boldsymbol{s}[t] \in \mathbb{C}^{N_t}$ is the signal dedicated for target sensing, whose covariance is $\mathbf{R}_s = \mathbb{E}\{\boldsymbol{s}[t]\boldsymbol{s}^H[t]\}$. The communication symbols have unit power and are independent and identically distributed (i.i.d) over time and users. Thus, we have $\mathbb{E}\{c_k[t]c_l^*[t]\} = \delta[k-l]$. The covariance of the transmitted signal $\boldsymbol{x}[t]$ is given by

$$\mathbf{R}_x = \mathbb{E}\{\boldsymbol{x}[t]\boldsymbol{x}^H[t]\} = \sum\nolimits_{k\in\mathcal{K}} \boldsymbol{f}_k\boldsymbol{f}_k^H + \mathbf{R}_s. \tag{2}$$

C. Communication model

We employ the near-field spherical wave model for the channels between the BS and users/targets. For a user $k \in \mathcal{K}$, the channel $\boldsymbol{h}_{t,k} \in \mathbb{C}^{N_t}$ is modeled as [12]:

$$[\boldsymbol{h}_{t,k}]_{n_t} = \sqrt{F(\boldsymbol{p}_k - \boldsymbol{p}_t(n_t), \boldsymbol{w}_t)}\beta(\boldsymbol{p}_k - \boldsymbol{p}_t(n_t)), \tag{3}$$

where $F(\boldsymbol{p}_k - \boldsymbol{p}_t(n_t), \boldsymbol{w}_t)$ is the radiation pattern (gain) of the antenna element. This function depends on the direction vector to the user, $\boldsymbol{p}_k - \boldsymbol{p}_t(n_t)$, and the antenna's radiation normal vector, $\boldsymbol{w}_t$. While the proposed framework is applicable to any antenna element model, for simulation purposes we adopt the commonly used cosine-based model from [13]:

$$F(\boldsymbol{p},\boldsymbol{w}) = \begin{cases} 2(b+1)\cos^b(\psi(\boldsymbol{p},\boldsymbol{w})), & \psi(\boldsymbol{p},\boldsymbol{w}) \in [0, \pi/2], \\ 0, & \text{otherwise}, \end{cases} \tag{4}$$

where $\psi(\boldsymbol{p}, \boldsymbol{w})$ is the angle between the direction vector $\boldsymbol{p}$ and the array's normal vector $\boldsymbol{w}$. The parameter b determines the Boresight gain, which is 2 for the dipole.

The term $\beta(\boldsymbol{p}_k - \boldsymbol{p}_t(i,l))$ denotes the attenuation and phase change caused by the path, with $\beta(\boldsymbol{p})$ being

$$\beta(\boldsymbol{p}) = \lambda/\left(4\pi\|\boldsymbol{p}\|\right) \cdot e^{-j\frac{2\pi}{\lambda}\|\boldsymbol{p}\|}. \tag{5}$$

Here, we compare the near-field model (3) to its far-field approximation. In the far-field case, the radiation profile and the path-loss term are both taken as constants across the array, i.e., $\sqrt{F(\boldsymbol{p}_k - \boldsymbol{p}_t(n_t), \boldsymbol{w}_t)} \approx \sqrt{F(\boldsymbol{p}_k - \boldsymbol{p}_{t,0}, \boldsymbol{w}_t)}$, $\lambda/(4\pi\|\boldsymbol{p}_k - \boldsymbol{p}_t(n_t)\|) \approx \lambda/(4\pi\|\boldsymbol{p}_k - \boldsymbol{p}_{t,0}\|)$, and the phase term uses the distance approximation as follows:

$$\begin{aligned}\left\|\boldsymbol{p}_k - \boldsymbol{p}_t(n_t)\right\| \approx\ & \left\|\boldsymbol{p}_k - \boldsymbol{p}_{t,0}\right\| - \left\|\boldsymbol{p}_t(n_t) - \boldsymbol{p}_{t,0}\right\| \\ & \times \cos(\psi(\boldsymbol{p}_t(n_t) - \boldsymbol{p}_{t,0},\, \boldsymbol{p}_k - \boldsymbol{p}_{t,0})) \\ \triangleq\ & \Delta_{n_t,k}.\end{aligned} \tag{6}$$

Hence the far-field channel becomes

$$\left[\boldsymbol{h}_{t,k}^{\text{far}}\right]_{n_t} = \sqrt{F(\boldsymbol{p}_k - \boldsymbol{p}_{t,0}, \boldsymbol{w}_t)}\, \beta(\boldsymbol{p}_k - \boldsymbol{p}_{t,0})\, e^{-j\frac{2\pi}{\lambda}\Delta_{n_t,k}}. \tag{7}$$

In the far-field model (7), the amplitude is a constant across all elements and the inter-element phase-differences depend only on the common directions in $\Delta_{n_t,k}$ and not on the distances. Consequently, far-field beamforming cannot resolve two users sharing the same angle but at different distances. In contrast, the near-field model (3) depends on the distance, indicating the capacity of distinguishing such users.

The received signal at user k at time t is

$$y_k[t] = \boldsymbol{h}_{t,k}^T\, \boldsymbol{x}[t] + n_k[t], \tag{8}$$

where $n_k[t] \sim \mathcal{CN}(0, \sigma_k^2)$ is the additive noise. Thus, the SINR at user k is given by:

$$\eta_k = \frac{\left|\boldsymbol{h}_{t,k}^T \boldsymbol{f}_k\right|^2}{\sum_{k' \in \mathcal{K}, k' \neq k} \left|\boldsymbol{h}_{t,k}^T \boldsymbol{f}_{k'}\right|^2 + \boldsymbol{h}_{t,k}^T \mathbf{R}_s \boldsymbol{h}_{t,k} + \sigma_k^2}. \tag{9}$$

The achievable communication rate for user k (in bits per second per Hz) is used as the performance metric, given by the Shannon capacity formula [12]:

$$R_k = \log_2(1 + \eta_k). \tag{10}$$

D. Sensing model

The sensing channel involves round-trip propagation to each target $l \in \mathcal{L}$, which can be separated into the forward channel (from the BS to the target) and the backward channel (from the target to the BS). Similarly to the near-field communication model (3), the forward channel $\boldsymbol{h}_{t,l} \in \mathbb{C}^{N_t}$ is modeled as

$$[\boldsymbol{h}_{t,l}]_{n_t} = \sqrt{F(\boldsymbol{p}_l - \boldsymbol{p}_t(n_t), \boldsymbol{w}_t)}\beta(\boldsymbol{p}_l - \boldsymbol{p}_t(n_t)), \tag{11}$$

and the backward channel $\boldsymbol{h}_{l,r} \in \mathbb{C}^{N_r}$ is modeled as

$$\left[\boldsymbol{h}_{l,r}\right]_{n_r} = \sqrt{F(\boldsymbol{p}_r(n_r) - \boldsymbol{p}_l, \boldsymbol{w}_r)}\beta(\boldsymbol{p}_r(n_r) - \boldsymbol{p}_l). \tag{12}$$

Thus, the overall round-trip sensing channel of target l, denoted as $\mathbf{H}_l \in \mathbb{C}^{N_r \times N_t}$ is given by

$$\mathbf{H}_l = \gamma_l \boldsymbol{h}_{l,r} \boldsymbol{h}_{t,l}^T, \tag{13}$$

where γ_l is the RCS of target l. Summing up the echoes of all targets, the received sensing signal at the BS is

$$\boldsymbol{y}_r[t] = \sum\nolimits_{l \in \mathcal{L}} \mathbf{H}_l \boldsymbol{x}[t] + \boldsymbol{n}_r[t], \tag{14}$$

where $\boldsymbol{n}_r[t] \sim \mathcal{CN}(\mathbf{0}, \sigma_r^2 \mathbf{I}_{N_r})$ is the sensing noise.

Similar to the communication case, the near-field sensing model in (13) also retains its dependence on distance, thereby enabling the resolution of targets at the same direction but different ranges.

For multi-target MIMO sensing, the transmit covariance $\mathbf{R}_x$ must be shaped to achieve two complementary objectives [8]–[10]: 1) **Beam-pattern gain**: maximize the power delivered to each target l, quantified by $\boldsymbol{h}_{t,l}^T \mathbf{R}_x \boldsymbol{h}_{t,l}^*$; 2) **Cross-correlation suppression**: minimize mutual interference between any two targets $l \neq l'$, quantified by $\left|\boldsymbol{h}_{t,l}^T \mathbf{R}_x \boldsymbol{h}_{t,l'}^*\right|$. This constraint ensures that the waveforms reflected from different targets are nearly orthogonal at the receiver, which is critical for distinguishing closely spaced targets and mitigating inter-target interference [10].

Remark: In multi-target sensing, existing far-field MIMO beamforming methods optimize beam-pattern and cross-correlation metrics exclusively over angular directions, treating each array's response as a planar wavefront that depends only on the angle [8]–[10]. More recent near-field study [3] extends beamforming to near-field spherical-wave channels but focuses on SINR-based designs that do not jointly shape angle-and-range beampatterns and suppress cross-correlation among multiple targets. As shown in Section IV, neglecting cross-correlation suppression makes classical MIMO techniques, e.g., Capon spectrum, incapable of indicating multiple targets. In contrast, our work is the first to generalize both beampattern and cross-correlation criteria to the near-field model, which accounts simultaneously for angle and distance; Thus it can resolve targets along the same direction but at different distances. Another advantage of our formulation is that the beam-pattern and cross-correlation metrics is independent of target RCSs knowledge, making it more broadly applicable compared to the SINR-based optimization in [3].

III. Beamforming Optimization

We formulate the joint beamforming design for multi-user communication and multi-target sensing as

$$\max_{\{\boldsymbol{f}_k\}, \mathbf{R}_s \succeq 0, \mathbf{R}_x, \mu} \quad \mu \tag{15a}$$

$$\text{s.t.} \quad w_l(\boldsymbol{h}_{t,l}^T \mathbf{R}_x \boldsymbol{h}_{t,l}^*) \geq \mu, \forall l \in \mathcal{L}, \tag{15b}$$

$$w_{l,l'}\left|\boldsymbol{h}_{t,l}^T \mathbf{R}_x \boldsymbol{h}_{t,l'}^*\right| \leq \varepsilon\mu, \forall l, l' \in \mathcal{L}, l \neq l', \tag{15c}$$

$$R_k \geq R_{\min,k}, \quad \forall k \in \mathcal{K}, \tag{15d}$$

$$\text{Tr}(\mathbf{R}_x) \leq P_{\max}, \tag{15e}$$

$$\mathbf{R}_x = \sum\nolimits_{k \in \mathcal{K}} \boldsymbol{f}_k \boldsymbol{f}_k^H + \mathbf{R}_s. \tag{15f}$$

Remark: While the mathematical structure of optimization (15) is general, its power is unlocked by using near-field channels. In far-field MIMO beamforming, metrics for beampattern gain and cross-correlation are optimized exclusively over angular directions. The key innovation and near-field specificity of our approach stem from the inputs used within this frame-

work—namely, the channel vectors $\boldsymbol{h}_{t,k}$ and $\boldsymbol{h}_{t,l}$. Because these vectors are defined by the spherical-wave model, they capture range-dependent phase and amplitude variations. This allows the beampattern and cross-correlation constraints, (15b) and (15c), to be enforced over a joint angle-range space. This is the core mechanism that enables our design to resolve co-directional users and targets, a task that is infeasible when using traditional far-field channel models within the same optimization structure.

The optimization in (15) maximizes an auxiliary variable μ, which represents the worst-case weighted sensing beampattern gain across all targets (objective (15a)), subject to the following: each target's weighted beampattern gain must be at least μ (constraint (15b)); the magnitude of the cross-correlation between any two targets, scaled by weight $w_{l,l'}$, must not exceed $\varepsilon\,\mu$ to suppress inter-target interference (constraint (15c)); each user's downlink rate must meet its minimum requirement $R_{\min,k}$ (constraint (15d)); the total transmit power must not exceed the budget $P_{\max}$ (constraint (15e)); and the overall transmit covariance $\mathbf{R}_x$ must equal the sum of the communication beamformer covariances and the sensing covariance as defined in (2) (constraint (15f)).

The optimization problem (15) is non-convex because of the quadratic term $\boldsymbol{f}_k\boldsymbol{f}_k^H$ in the equality constraint (15f). To solve it, we recast it into a convex optimization using the SDR strategy following the two steps below.

First, using the Shannon capacity formula (10) and the definition of SINR (9), (15d) is equivalent to [2]

$$\mathrm{Tr}\Big(\boldsymbol{h}_{t,k}^*\,\boldsymbol{h}_{t,k}^T\big(\,\xi_k\,\boldsymbol{f}_k\,\boldsymbol{f}_k^H-\mathbf{R}_x\big)\Big)\geq\sigma_k^2, \tag{16}$$

where $\xi_k=2^{\,R_{\min,k}}/(2^{R_{\min,k}}-1)$.

Second, we replace the optimized variable $\boldsymbol{f}_k$ with $\mathbf{F}_k=\boldsymbol{f}_k\boldsymbol{f}_k^H$ and leave out the constraint that $\mathbf{F}_k$ is rank-one. Thus, the optimization (15) is relaxed to

$$\max_{\{\mathbf{F}_k\},\mathbf{R}_s\succeq 0,\mathbf{R}_x,\mu}\quad \mu \tag{17a}$$

$$\text{s.t.}\quad w_l(\boldsymbol{h}_{t,l}^T\mathbf{R}_x\boldsymbol{h}_{t,l}^*)\geq\mu,\ \forall l\in\mathcal{L}, \tag{17b}$$

$$w_{l,l'}\big|\boldsymbol{h}_{t,l}^T\mathbf{R}_x\boldsymbol{h}_{t,l'}^*\big|\leq\varepsilon\mu,\forall l,l'\in\mathcal{L},l\neq l', \tag{17c}$$

$$\mathrm{Tr}\left(\boldsymbol{h}_{t,k}^*\boldsymbol{h}_{t,k}^T(\xi_k\mathbf{F}_k-\mathbf{R}_x)\right)\geq\sigma_k^2,\forall k\in\mathcal{K}, \tag{17d}$$

$$\mathrm{Tr}(\mathbf{R}_x)\leq P_{\max}, \tag{17e}$$

$$\mathbf{R}_x=\sum\nolimits_{k\in\mathcal{K}}\mathbf{F}_k+\mathbf{R}_s. \tag{17f}$$

The relaxed optimization (17) is convex and can be solved with cvx in MATLAB. The optimum is denoted as $\{\hat{\mathbf{F}}_k\}_{k\in\mathcal{K}}$ and $\hat{\mathbf{R}}_s$. We can construct the following rank-one solution that achieves the same objective value without violating the constraints of (15) [8, Theorem 1]:

$$\tilde{\boldsymbol{f}}_k=\left(\boldsymbol{h}_{t,k}^T\hat{\mathbf{F}}_k\boldsymbol{h}_{t,k}^*\right)^{-1/2}\hat{\mathbf{F}}_k\boldsymbol{h}_{t,k}^*. \tag{18}$$

Proof. By [8, Theorem 1], $\tilde{\boldsymbol{f}}_k\tilde{\boldsymbol{f}}_k^H\preceq\hat{\mathbf{F}}_k$. Hence if we set

$$\tilde{\mathbf{R}}_s\;=\;\hat{\mathbf{R}}_s\;+\;\sum_{k=1}^{K}\Big(\hat{\mathbf{F}}_k-\tilde{\boldsymbol{f}}_k\tilde{\boldsymbol{f}}_k^H\Big),$$

then $\tilde{\mathbf{R}}_s\succeq\mathbf{0}$ and the total transmit covariance based on $\{\tilde{\boldsymbol{f}}_k\}$ and $\tilde{\mathbf{R}}_s$ is unchanged. Thus, the constraints (15b), (15c) and (15e) remain satisfied. Moreover, [8, Theorem 1] shows that $\left|\boldsymbol{h}_{t,k}^T\tilde{\boldsymbol{f}}_k\right|^2=\boldsymbol{h}_{t,k}^T\hat{\mathbf{F}}_k\,\boldsymbol{h}_{t,k}^*$, so all the SINR constraints (16) remain satisfied, making the rate constraints (15d) satisfied. Thus, $\{\tilde{\boldsymbol{f}}_k\}$ and $\tilde{\mathbf{R}}_s$ form a feasible rank-one solution with the same objective. □

IV. Simulation Results

In this section, we evaluate the performance of the proposed near-field ISAC beamforming design via numerical simulations. Specifically, we compare our method against two benchmarks: no cross-correlation suppression (NCCS), which omits the cross-correlation suppression constraint, and far-field beamforming (FFBF), which employs a far-field beamforming model. We will demonstrate gains in both downlink communication (SINR and achievable rate) and multi-target sensing (Capon spectrum) under mmWave configurations.

A. Parameter and method configurations

The operating frequency is $f_c=30$ GHz, corresponding to a wavelength of $\lambda=10$ mm. The transmit power at the BS is $P_{\max}=23$ dBm, while the noise power is configured as $\sigma^2=-80$ dBm for the BS receiver and all the communication users. The block length is $T=1000$.

The transmitting and receiving arrays of the BS are both uniform planar arrays (UPAs) with $N_t=10\times10$ elements, where the inter-element spacing is $\lambda/2$. The corresponding Rayleigh distance of near-field region is $R_{\text{RL}}=1$ m, where the antenna aperture is given by $D=0.071$ m. The BS transmitter and receiver are centered at $\boldsymbol{p}_t=(0,0,0)$ m and $\boldsymbol{p}_t=(0,0.06,0)$ m, whose radiation normal vectors are both $\boldsymbol{w}_t=(0,0,1)$.

The number of communication users is $K=2$, indexed as User 1 and 2, whose positions are $(0,0.1,0.1)$ m and $(0,0.5,0.5)$ m, respectively. The number of sensing targets is $L=3$, indexed as Target 1, 2 and 3, whose positions are $(0,-0.1,0.1)$ m, $(0,-0.25,0.25)$ m and $(0,0,0.4)$ m, respectively. The RCSs of targets are all 1. Note that User 1 and User 2 locate along the same direction from the BS transmitter but at different ranges, as do Targets 1 and 2.

In the optimization (15), we set a minimum rate requirement of $R_{\min}=17$ bps/Hz for both users. In beam-pattern and cross-correlation constraints, i.e., (15b) and (15c), we set the weights as $w_l=1/\|\boldsymbol{h}_{t,l}\|^2$ and $w_{l,l'}=1/(\|\boldsymbol{h}_{t,l}\|\cdot\|\boldsymbol{h}_{t,l'}\|)$, respectively, to balance the sensing requirements across all targets regardless of their individual channel strengths. The cross-correlation tolerance parameter is $\varepsilon=0.1$.

In addition, we consider two benchmark schemes for comparison: 1) **NCCS**: We solve the same problem as (15) but omit constraint (15c), thus removing the

cross-correlation suppression on multi-target sensing. 2) **FFBF**: To highlight the benefits of near-field design, we solve (15) after replacing every channel vector $\boldsymbol{h}_{t,a}$ ($a \in \mathcal{K} \cup \mathcal{L}$) with its far-field approximation (7). Additionally, since far-field users or targets at the same direction become fully coherent, we relax the communication constraint by lowering $R_{\min}$ to 0.95 bps/Hz and remove the cross-correlation constraint (15d) for the target pair $(1, 2)$, thereby ensuring problem feasibility. Note that if we set $R_{1,\min} = R_{2,\min} = R_{\min}$, the optimization is feasible only if $R_{\min} < 1$ bps/Hz in far-field modeling.

B. Communication performance

To showcase the spatial discrimination enabled by our near-field design, Fig. 2, 3 and 4 plot each user's SINR over the entire yz–plane under the proposed method, NCCS, and FFBF, respectively. In both the proposed and NCCS schemes (Fig. 2, 3), each user's SINR exhibits a sharp peak at its location and deep nulls at the other user's location, confirming the ability to resolve users aligned in the same direction but at different distances. By contrast, the far-field beamforming in Fig. 4 produces overlapping SINR patterns that cannot distinguish users along the same direction but at different distances; Moreover, the peak SINR remains below 0 dB, far weaker than the above 40 dB peaks achieved by the near-field approaches. Such SINR level renders reliable communication impossible, thus highlighting the advantage of near-field ISAC beamforming for multi-user separation.

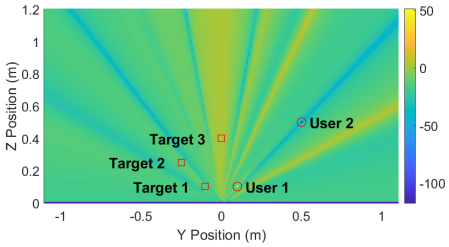

(a) User 1's received power over the yz–plane

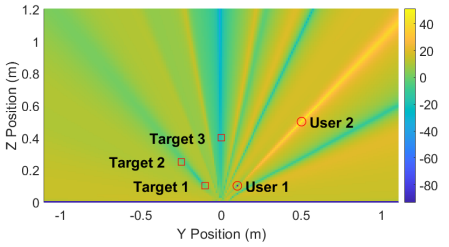

(b) User 2's received power over the yz–plane

Fig. 2: SINR (in dB) of each user's downlink signal over the yz-plane with proposed method.

C. Sensing performance

In this section, we examine the localization performance with the Capon spectrum. First, we generate the sensing signal using (14). Then, for any position $\boldsymbol{p}_0$, the normalized Capon spectrum is given by [14]

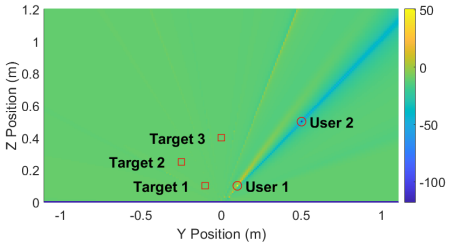

(a) User 1's received power over the yz–plane

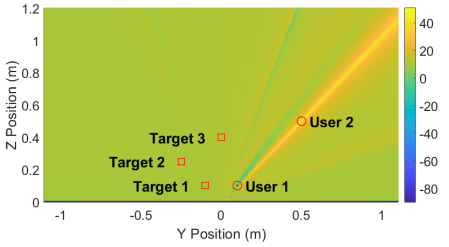

(b) User 2's received power over the yz–plane

Fig. 3: SINR (in dB) of each user's downlink signal over the yz-plane with NCCS.

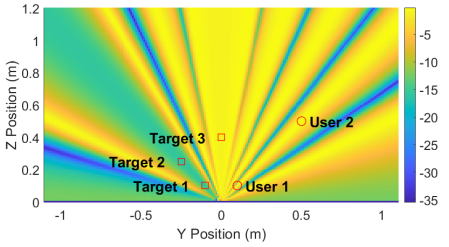

(a) User 1's received power over the yz–plane

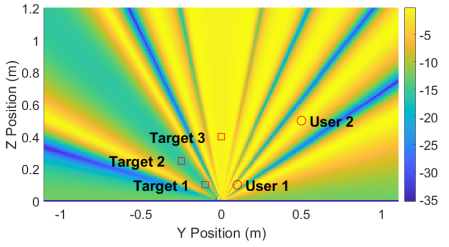

(b) User 2's received power over the yz–plane

Fig. 4: SINR (in dB) of each user's downlink signal over the yz-plane with FFBF.

$$\beta_{\text{capon}}(\boldsymbol{p}_0) = \frac{\tilde{\boldsymbol{h}}_{0,r}^H \mathbf{R}_Y^{-1} \mathbf{Y}\mathbf{X}^H \tilde{\boldsymbol{h}}_{t,0}^*}{T(\tilde{\boldsymbol{h}}_{0,r}^H \mathbf{R}_Y^{-1} \tilde{\boldsymbol{h}}_{0,r})(\tilde{\boldsymbol{h}}_{l,0}^T \mathbf{R}_X^{-1} \tilde{\boldsymbol{h}}_{l,0}^*)}. \quad (19)$$

Here $\mathbf{X} = [\boldsymbol{x}[1], \ldots, \boldsymbol{x}[T]]$ and $\mathbf{Y} = [\boldsymbol{y}[1], \ldots, \boldsymbol{y}[T]]$ collect the transmitted and received snapshots, and $\mathbf{R}_X = \frac{1}{T}\mathbf{X}\mathbf{X}^H$, $\mathbf{R}_Y = \frac{1}{T}\mathbf{Y}\mathbf{Y}^H$ are their sample covariance matrices. The normalized steering vectors $\tilde{\boldsymbol{h}}_{t,0} = \boldsymbol{h}_{t,0}/\|\boldsymbol{h}_{t,0}\|$ and $\tilde{\boldsymbol{h}}_{0,r} = \boldsymbol{h}_{0,r}/\|\boldsymbol{h}_{0,r}\|$ are formed by evaluating (11) and (12) at $\boldsymbol{p}_0$ and then normalizing. Compared to the conventional Capon spectrum, (19) employs normalized vectors to remove range-dependent amplitude scaling.

Fig. 5 plots the normalized Capon spectrum over the yz–plane for the proposed method, NCCS, and FFBF. In

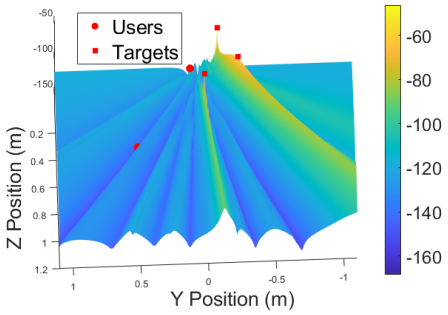

(a) Normalized Capon spectrum (in dB) with proposed method

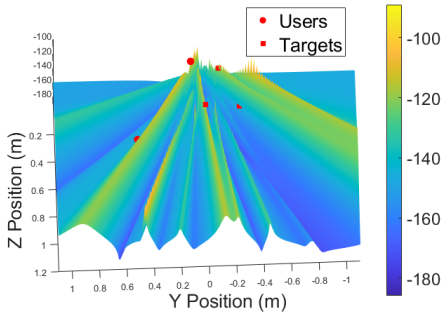

(b) Normalized Capon spectrum (in dB) with NCCS

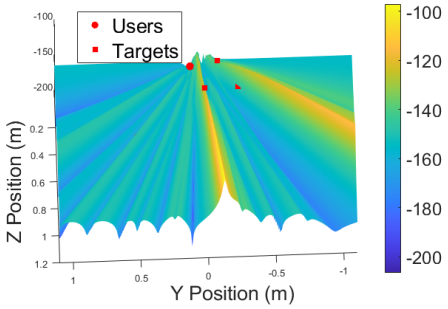

(c) Normalized Capon spectrum (in dB) with FFBF

Fig. 5: Normalized Capon spectrum (in dB) of sensing with (a) proposed method, (b) NCCS, (c) FFBF.

Fig. 5a, three distinct peaks arise exactly at the true positions of Targets 1–3, confirming that our near-field beamformer can capture both angular and range information and separates targets along the same direction (Targets 1 and 2). By contrast, Fig. 5b yields a cluttered spectrum with spurious peaks and no clear target signatures, illustrating that neglecting cross-correlation suppression renders classical Capon processing ineffective in multi-target scenarios. Finally, Fig. 5c cannot distinguish target distances—it shows only angular lobes—and it merges Targets 1 and 2 into a single peak. This highlights the far-field model's inability to resolve targets along the same direction in range or combined angle–range domains. Overall, these results underscore the clear advantage of our joint beampattern and cross-correlation optimization in near-field ISAC for precise multi-target localization.

V. Conclusion

In this paper, we developed a beamforming strategy for near-field ISAC systems that serves multiple downlink users and senses multiple targets without requiring prior RCS information. By formulating a max–min beampattern gain optimization with cross-correlation suppression, per-user rate guarantees, and total power limits, we extended classical far-field metrics to jointly account for angle and range. Such an extension enabled the separation of objects along the same direction but at different distances. The original non-convex design was relaxed into a semidefinite program, and we proposed a simple rank-one reconstruction yielding closed-form beamformers that attain the global optimum. Numerical results demonstrated that our approach substantially outperforms both no cross-correlation suppression and far-field benchmarks in terms of communication rate and multi-target localization accuracy.

References

[1] F. Liu, Y. Cui, C. Masouros, J. Xu, T. X. Han, Y. C. Eldar, and S. Buzzi, "Integrated sensing and communications: Toward dual-functional wireless networks for 6G and beyond," *IEEE J. Sel. Areas Commun.*, vol. 40, no. 6, pp. 1728–1767, 2022.

[2] Z. Wang, X. Mu, and Y. Liu, "Near-field integrated sensing and communications," *IEEE Commun. Lett.*, vol. 27, no. 8, pp. 2048–2052, 2023.

[3] D. Galappaththige, S. Zargari, C. Tellambura, and G. Y. Li, "Near-field ISAC: Beamforming for multi-target detection," *IEEE Wireless Commun. Lett.*, 2024.

[4] K. Qu, S. Guo, N. Saeed, and J. Ye, "Near-field integrated sensing and communication: Performance analysis and beamforming design," *IEEE Open J. Commun. Soc.*, 2024.

[5] B. Zhao, C. Ouyang, Y. Liu, X. Zhang, and H. V. Poor, "Modeling and analysis of near-field ISAC," *IEEE J. Sel. Top. Signal Process.*, 2024.

[6] H. Li, Z. Wang, X. Mu, Z. Pan, and Y. Liu, "Near-field integrated sensing, positioning, and communication: A downlink and uplink framework," *IEEE J. Sel. Areas Commun.*, 2024.

[7] H. Hua, J. Xu, and R. Zhang, "Near-field integrated sensing and communication with extremely large-scale antenna array," *IEEE Trans. Wireless Commun.*, 2025.

[8] X. Liu, T. Huang, N. Shlezinger, Y. Liu, J. Zhou, and Y. C. Eldar, "Joint transmit beamforming for multiuser MIMO communications and MIMO radar," *IEEE Trans. Signal Process.*, vol. 68, pp. 3929–3944, 2020.

[9] C. Meng, Z. Wei, D. Ma, W. Ni, L. Su, and Z. Feng, "Multi-objective optimization-based transmit beamforming for multi-target and multi-user MIMO-ISAC systems," *IEEE Internet Things J.*, 2024.

[10] P. Stoica, J. Li, and Y. Xie, "On probing signal design for MIMO radar," *IEEE Trans. Signal Process.*, vol. 55, no. 8, pp. 4151–4161, 2007.

[11] H. Hua, J. Xu, and T. X. Han, "Optimal transmit beamforming for integrated sensing and communication," *IEEE Trans. Veh. Technol.*, vol. 72, no. 8, pp. 10 588–10 603, 2023.

[12] H. Zhang, N. Shlezinger, F. Guidi, D. Dardari, M. F. Imani, and Y. C. Eldar, "Beam focusing for near-field multiuser MIMO communications," *IEEE Trans. Wireless Commun.*, vol. 21, no. 9, pp. 7476–7490, 2022.

[13] S. W. Ellingson, "Path loss in reconfigurable intelligent surface-enabled channels," in *Proc. IEEE 32nd Annu. Int. Symp. Pers., Indoor Mobile Radio Commun. (PIMRC)*, 2021, pp. 829–835.

[14] L. Xu, J. Li, and P. Stoica, "Target detection and parameter estimation for MIMO radar systems," *IEEE Trans. Aerosp. Electron. Syst.*, vol. 44, no. 3, pp. 927–939, 2008.